Meteoritics & Planetary Science 39, Nr 3, 407–424 (2004)
Abstract available online at http://meteoritics.org

Radar observations of asteroid 25143 Itokawa (1998 SF36)

Steven J. OSTRO,[1*] Lance A. M. BENNER,[1] Michael C. NOLAN,[2] Christopher MAGRI,[3]
Jon D. GIORGINI,[1] Daniel J. SCHEERES,[4] Stephen B. BROSCHART,[4] Mikko KAASALAINEN,[5]
David VOKROUHLICKÝ,[6] Steven R. CHESLEY,[1] Jean-Luc MARGOT,[7] Raymond F. JURGENS,[1]
Randy ROSE,[1] Donald K. YEOMANS,[1] Shigeru SUZUKI,[1] and Eric M. DE JONG[1]

[1]Jet Propulsion Laboratory, California Institute of Technology, Pasadena, California 91109–8099, USA
[2]Arecibo Observatory, HC3 Box 53995, Arecibo, Puerto Rico 00612, USA
[3]University of Maine at Farmington, 173 High Street, Preble Hall, Farmington, Maine 04938, USA
[4]Department of Aerospace Engineering, University of Michigan, Ann Arbor, Michigan 48109–2140, USA
[5]Rolf Nevanlinna Institute, University of Helsinki, P. O. Box 4, FIN-00014 Helsinki, Finland, and Sodankyla Geophysical Observatory,
University of Oulu, Tahtelantie 62, FIN-99600 Sodankyla, Finland
[6]Institute of Astronomy, Charles University, V Holešovičkách 2, CZ-180 00 Prague 8, The Czech Republic
[7]Department of Earth and Space Sciences, University of California, Los Angeles, 595 Charles Young Drive East,
3806 Geology Building, Los Angeles, California 90095–1567, USA
[*]Corresponding author. E-mail: ostro@reason.jpl.nasa.gov

(Received 14 November 2003; revision accepted 22 January 2004)

Abstract–We observed 25143 Itokawa, the target of Japan's Hayabusa (MUSES-C) sample-return mission, during its 2001 close approach at Arecibo on twelve dates during March 18–April 9 and at Goldstone on nine dates during March 20–April 2. We obtained delay-Doppler images with range resolutions of 100 ns (15 m) at Arecibo and 125 ns (19 m) at Goldstone. Itokawa's average circular polarization ratio at 13 cm, 0.26 ± 0.04, is comparable to that of Eros, so its cm-to-m surface roughness probably is comparable to that on Eros. Itokawa's radar reflectivity and polarization properties indicate a near-surface bulk density within 20% of 2.5 g cm^{-3}. We present a preliminary estimate of Itokawa's shape, reconstructed from images with rather limited rotation-phase coverage, using the method of Hudson (1993) and assuming the lightcurve-derived spin period (12.132 hr) and pole direction (ecliptic long., lat. = 355°, –84°) of Kaasalainen et al. (2003). The model can be described as a slightly asymmetrical, slightly flattened ellipsoid with extents along its principal axes of 548 × 312 × 276 m ± 10%. Itokawa's topography is very subdued compared to that of other asteroids for which spacecraft images or radar reconstructions are available. Similarly, gravitational slopes on our Itokawa model average only 9° and everywhere are less than 27°. The radar-refined orbit allows accurate identification of Itokawa's close planetary approaches through 2170. If radar ranging planned for Itokawa's 2004 apparition succeeds, then tracking of Hayabusa during its 2005 rendezvous should reveal Yarkovsky perturbation of the asteroid's orbit.

INTRODUCTION

Asteroid 25143 Itokawa (1998 SF36) was discovered on September 26, 1998, by LINEAR (MPEC 1998-S45). Of the more than 1000 currently known near-Earth asteroids (NEAs) at least as bright (that is, with absolute magnitude H <18.8), Itokawa is distinguished by having the lowest delta-V for a spacecraft rendezvous: 4.29 km s^{-1} versus 5.95 for 433 Eros. Because of this attribute, Itokawa was selected as the target of Japan's Hayabusa (formerly MUSES-C) mission to return a sample from an asteroid. The Hayabusa spacecraft is en route to a June 2005 rendezvous and a June 2007 return to Earth.

Visible and near-infrared spectroscopy (Binzel et al. 2001; see also Dermawan et al. 2002 and Sekiguchi et al. 2003) suggested that Itokawa has a surface composition like that of ordinary chondrite meteorites and is most similar in spectral characteristics and modeled olivine/pyroxene content to the LL chondrite class. Kaasalainen et al. (2003, henceforth K+2003) present photometry and an analysis yielding estimates of the asteroid's sidereal spin period, P = 12.132 ± 0.0005 hr, and pole direction: ecliptic long., lat. = 355°, –84° ± 5°. They estimated a three-dimensional shape, concluding that Itokawa is "elongated, with rough global dimension ratios a/b = 2.0, b/c = 1.3, but the elongation is not due to a bifurcated shape. The surface is not likely to contain major concavities. No significant albedo variegation was detected."

Here we report radar observations carried out during March–April 2001 at Arecibo and Goldstone. As illustrated in Fig. 1 and Table 1, the asteroid's closest approach was at declination +15°, within several degrees of Arecibo's latitude and hence the middle of its declination window. This geometry meant that Goldstone, despite its full steerability, could not supplement the sky arc observable by Arecibo. However, in late February 2001, just weeks before the closest approach, it was discovered by several groups of observers (see list in K+2003) that the asteroid's rotation period was close to half a day. Since Arecibo can only view within 20° of the zenith, and hence cannot observe a target for more than 2.7 hr per day, that rotation period meant that Arecibo would see no more than one-fifth of a rotation on each date, with little day-to-day phase migration. We requested Goldstone tracks on very short notice, and due to the generosity of numerous NASA projects, enough time on the 70-m antenna, DSS-14, was made available to ensure thorough rotation phase coverage.

We completed about 2800 transmit-receive cycles (runs), more than 2700 of which were for high-resolution imaging. Tables 2 and 3 give the experiment's masterlogs. Our techniques of observation, data reduction, data analysis, and inference of physical properties were similar to those described most recently by Ostro et al. (2001) and references therein. We began each track with a few continuous-wave (cw) runs that produced Doppler-only images (power spectra) almost in real time, letting us check that the entire radar system was working, but most of our observations used binary phase-coded waveforms to produce delay-Doppler images. All our Arecibo observations and all our Goldstone cw observations used reception in the same circular (SC) polarization as transmitted as well as the opposite circular (OC); the circular polarization ratio, SC/OC, is a measure of near-surface structural complexity at scales within an order of magnitude of the wavelength.

Delay-Doppler images are time exposures. One image, or look, with frequency resolution Δf requires Fourier analysis of a coherent, complex-voltage time series of duration $1/\Delta f$. A single look is intrinsically noisy. Incoherent summation of N looks reduces the noise by a factor of $N^{-1/2}$ while compromising spatial resolution because of rotational smear. Exactly how to strike the balance between spatial resolution and noise is a subjective judgment call. For Itokawa, our analyses used values of N = 20 for Goldstone, corresponding to ~13° of phase smearing, and 4–10 for Arecibo, corresponding to 3–7° of phase smearing.

RADAR ASTROMETRY AND ORBIT REFINEMENT

At several points in the experiment, especially during its first half, we used our radar astrometry along with any available optical astrometry to refine the asteroid's orbit and

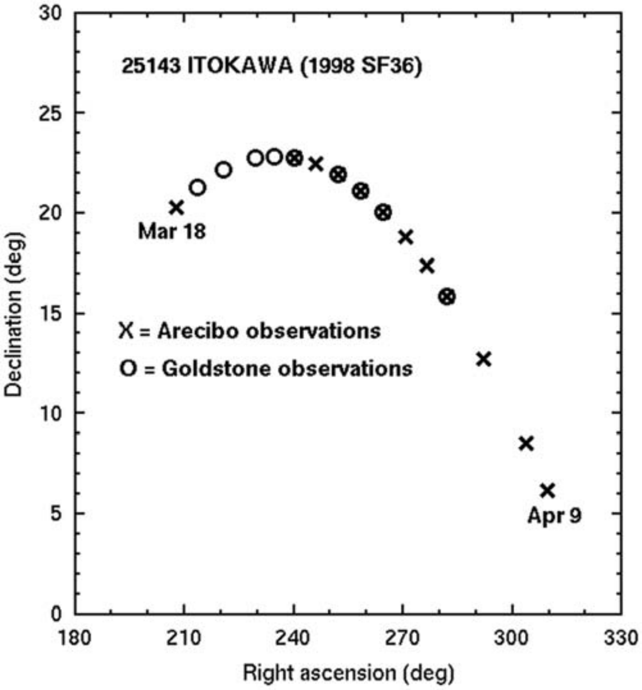

Fig. 1. Itokawa's sky location at 00:00 UTC on each date of the radar observations.

Table 1. Right ascension, declination, distance, and predicted signal-to-noise ratio per run for Itokawa radar observations, at 00:00 on each UTC date.

Date	RA (deg)	Decl (deg)	Dist. (AU)	Goldstone SNR	Arecibo SNR
2001 Mar 18	215	17	0.062	8	320
2001 Mar 19	218	17	0.059	9	380
2001 Mar 20	221	17	0.056	11	450
2001 Mar 21	225	17	0.053	13	530
2001 Mar 22	229	18	0.051	15	630
2001 Mar 23	233	17	0.049	18	720
2001 Mar 24	238	17	0.047	20	830
2001 Mar 25	243	17	0.046	23	920
2001 Mar 26	248	17	0.044	25	1000
2001 Mar 27	254	16	0.044	26	1100
2001 Mar 28	259	15	0.043	27	1100
2001 Mar 29	265	14	0.043	27	1100
2001 Mar 30	270	13	0.044	26	1100
2001 Mar 31	276	12	0.044	25	1000
2001 Apr 01	281	11	0.046	23	930
2001 Apr 02	285	10	0.047	20	840
2001 Apr 03	290	8	0.049	18	740
2001 Apr 04	294	7	0.051	16	640
2001 Apr 05	297	6	0.053	14	550
2001 Apr 06	301	5	0.055	12	470
2001 Apr 07	304	4	0.058	10	400
2001 Apr 08	307	3	0.060	8	340
2001 Apr 09	309	2	0.063	7	270
2001 Apr 10	312	2	0.066	6	220

Table 2. Imaging masterlog. Here DOY is day of year and RTT is the echo's roundtrip time delay. For each date, we give the code length for the (repetitive) binary-phase-coded transmission, the delay resolution (baud), the frequency resolution of reduced images, the OSOD orbit solution number, the number of runs, the first and last times of data reception (UTC), and the subradar track's latitude and rotation-phase (west longitude) range. Arecibo data was taken with the Radar Interface on March 18 and by the Caltech Baseband Recorder (CBR, for a total of 979 runs) on the other dates.

				Baud	Fres			rcsta rcend	Subradar	
2001	DOY	RTT	Code	(ns)	(Hz)	OSOD	Runs	HHMMSS–HHMMSS	lat.	long.
Arecibo										
Mar 18	077	60	16383	500	0.060	30	62	055716–080009	35	110–160
Mar 26	085	40	65535	100	0.065	42	24	072305–091632	46	135–183
Mar 27	086	39	65535	100	0.065	42	117	073853–100111	46	141–207
Mar 28	087	38	65535	100	0.065	44	90	085621–102317	45	150–218
Mar 29	088	38	65535	100	0.065	48	107	082324–104635	44	165–231
Mar 30	089	38	65535	100	0.065	50	112	083827–110658	43	174–241
Mar 31	090	39	65535	100	0.065	50	99	091535–112703	41	192–252
Apr 01	091	40	65535	100	0.065	50	93	092853–114617	38	198–262
Apr 02	092	41	65535	100	0.065	50	108	092835–120229	35	198–268
Apr 04	094	44	65535	100	0.065	50	91	100606–122334	30	211–275
Apr 07	097	51	65535	100	0.065	52	81	103536–125308	22	217–276
Apr 09	099	57	65535	100	0.065	52	57	110838–125758	18	221–270
							1041			
Goldstone										
Mar 20	079	53	127	250	1.000	36	64	132523–153045	39	319–22
Mar 22	081	48	127	125	0.500	36, 38	128	101337–145608	41	218–359
Mar 24	083	43	127	125	0.250	40	21	141913–145007	44	338–353
Mar 25	084	42	127	125	0.250	40	160	085749–130819	45	176–302
Mar 26	085	40	127	125	0.250	42	211	083331–144547	46	165–351
Mar 28	087	38	127	125	0.250	44	189	091256–144101	45	186–350
Mar 29	088	38	127	125	0.250	48	273	082613–145425	44	164–358
Mar 30	089	38	127	125	0.250	50	362	083715–172036	42	180–66
Apr 2	092	41	127	125	0.250	50	253	092001–160012	35	190–29
							1661			

Table 3. Radar cross section estimates from Arecibo cw spectra. Columns give the number of cw runs on each date, estimates of the OC and SC radar cross sections, the subradar latitude and west longitude, the model projected area, the OC and SC radar albedos obtained by dividing the cross section by the projected area, and the circular polarization ratio SC/OC. Some of the dispersion in our estimates of radar properties is probably due to systematic error.

		Radar cross section (km^2 ± 25%)		Subradar		Radar albedo		
2001	CW runs	OC	SC	lat, long	Proj. area	OC	SC	SC/OC
Mar 18	2	0.0164	0.00428	36, 58	0.1185	0.134	0.035	0.261
Mar 26	11	0.0195	0.00529	48, 96	0.1306	0.160	0.044	0.271
Mar 27	11	0.0233	0.00479	48, 105	0.1295	0.196	0.040	0.206
Mar 28	11	0.0180	0.00498	48, 117	0.1270	0.156	0.043	0.276
Mar 29	11	0.0183	0.00518	47, 131	0.1222	0.166	0.047	0.283
Mar 30	11	0.0186	0.00490	45, 140	0.1176	0.174	0.046	0.264
Mar 31	5	0.0211	0.00488	43, 161	0.1090	0.205	0.047	0.231
Apr 01	5	0.0208	0.00437	41, 181	0.1034	0.199	0.042	0.210
Apr 02	5	0.0136	0.00471	38, 167	0.1015	0.141	0.049	0.346
Apr 04	5	0.0149	0.00395	32, 181	0.0918	0.155	0.041	0.265
Apr 09	5	0.0110	0.00234	21, 161	0.0833	0.118	0.025	0.213
Mean						0.164	0.042	0.257
±r.m.s.						0.027	0.007	0.040
Range						0.087	0.024	0.140
Adopted values and standard errors:								
SC/OC ratio		0.26 ± 0.04						
OC albedo		0.16 ± 0.05						

our delay-Doppler prediction ephemerides. It was clear from the first few tracks that Itokawa is an elongated asteroid. In refining the orbit, we used radar astrometry referenced to the asteroid's center of mass (COM), subjectively estimating the COM's location from inspection of the echoes and assigning very conservative uncertainties to the measurements. We used JPL's On-Site Orbit Determination program (OSOD) to generate all ephemerides used for this experiment. Prior to our first observation, the formal, 1σ uncertainties in the ephemeris (OSOD solution #30) were 4 arcsec, 5 cm s^{-1} in radial velocity, and 1.33 milliseconds in time delay (200 km in range). By the last week of the experiment, we had shrunk them to 0.4 arcsec, 0.7 mm s^{-1}, and 3 microseconds (<0.5 km, approximately the size of the asteroid).

In modeling the shape of Itokawa (see below), the COM's motion through the images is estimated along with the object's physical properties. We have used the resultant delay-Doppler astrometry (Table 4) along with available optical astrometry to refine the object's orbit (Table 5), which allows accurate identification of Itokawa's close planetary approaches over the 380-yr interval from 1790 to 2170 (Table 6). This prediction window is atypically short for such a well-observed asteroid, perhaps due to its generally slower than usual encounter velocities with Earth and Mars (5–8 km s^{-1} versus more typical values of about 14 km s^{-1}), which give each planetary encounter a relatively long time to affect the orbit statistical uncertainties, causing them to increase.

IMAGING RESULTS

Figures 2 and 3 show most of our images averaged over time spans that strike a reasonable balance between maximizing both the signal-to-noise level (which improves as the square root of the time span) and rotational smearing. The Goldstone tracks were longer and, hence, provided greater rotation-phase coverage, while the Arecibo echoes are much stronger.

The variations in bandwidth and delay depth of Itokawa's echoes indicated that the object is roughly twice as long as it is wide; see, for example, the March 30 Goldstone collage (Fig. 3), which spans nearly 3/4 of a rotation. Moreover, the roughly two-fold variation in both delay depth and bandwidth indicated that the radar view was closer to equatorial than pole-on.

Table 4. Itokawa radar astrometry. Entries give estimates of the roundtrip time delay and Doppler frequency for echoes from Itokawa's COM received at the indicated UTC epoch, as determined as part of the shape-modeling process. The reference point for Arecibo (A) is the main antenna's center of curvature. The reference point for Goldstone (G) is the intersection of azimuth and elevation axes of the 70-m antenna, DSS-14. For each observation, the same antenna was used for transmitting and receiving. Estimated standard errors in the astrometry reflect the imaging resolution and the echo strength.

UTC date YYYYMMDD	HHMMSS	Obs.	Data type	Measurement	Residual (sol #74)
20010409	111400	A	Delay	56.49679409 s ± 100 ns	–60 ns
20010407	104600	A	Delay	50.97948692 s ± 100 ns	–20 ns
20010404	101100	A	Delay	44.06019264 s ± 100 ns	141 ns
20010402	093700	A	Delay	40.68912931 s ± 100 ns	–9 ns
20010401	093400	A	Delay	39.49645726 s ± 100 ns	23 ns
20010331	092000	A	Delay	38.65875907 s ± 100 ns	–26 ns
20010330	090000	G	Delay	38.22863568 s ± 250 ns	203 ns
20010330	084400	A	Delay	38.20880739 s ± 100 ns	–29 ns
20010329	082900	A	Delay	38.17475069 s ± 100 ns	–42 ns
20010328	080100	A	Delay	38.55786088 s ± 100 ns	–57 ns
20010327	074500	A	Delay	39.34265233 s ± 100 ns	78 ns
20010326	073500	A	Delay	40.50596341 s ± 100 ns	–44 ns
20010318	060700	A	Delay	59.94966397 s ± 500 ns	609 ns
20010409	120000	A	Doppler	–79160.53 Hz ± 60 mHz	–46 mHz
20010407	114800	A	Doppler	–71393.26 Hz ± 60 mHz	–47 mHz
20010404	111900	A	Doppler	–54244.53 Hz ± 60 mHz	–31 mHz
20010402	105400	A	Doppler	–38271.80 Hz ± 60 mHz	–56 mHz
20010401	105200	A	Doppler	–29298.16 Hz ± 60 mHz	–49 mHz
20010331	102700	A	Doppler	–18741.98 Hz ± 60 mHz	–60 mHz
20010330	125000	G	Doppler	–28726.76 Hz ± 500 mHz	93 mHz
20010330	095600	A	Doppler	–7406.385 Hz ± 60 mHz	–41 mHz
20010329	094100	A	Doppler	3636.498 Hz ± 60 mHz	–39 mHz
20010328	092000	A	Doppler	14841.96 Hz ± 60 mHz	–30 mHz
20010327	085800	A	Doppler	25717.34 Hz ± 60 mHz	–33 mHz
20010326	083600	A	Doppler	35971.48 Hz ± 60 mHz	–30 mHz
20010318	065800	A	Doppler	87291.569 Hz ± 60 mHz	40 mHz

Table 5. Itokawa orbit solution number 74 with estimated formal uncertainties at the solution epoch 2001-Sep-27.0 (Coordinate Time). The optical data consisted of 623 usable measurements spanning 1998-Sep-25 to 2001-Sep-20, with post-fit residual mean and root mean square (rms) of (0.240, 0.508) arcsec. The normalized rms (n-rms), obtained by first dividing each measurement by its assigned uncertainty, is 0.498. Optical data was generally weighted at 1 arcsec except for data reported by site 921, which was deweighted to 2.0 arcsec. For radar delay, the residual mean and rms are (62, 186) ns and n-rms is 0.695. For Doppler frequency, the residual mean and rms are (−0.025, 0.049) Hz and n-rms is 0.690. The combined data-type n-rms is 0.503. Elements are in the ICRF93/J2000 coordinate frame of the DE-403 JPL planetary ephemeris, a quasar-based radio frame within 0.2 to 0.05 arcsec of the optical FK5/J2000. Angular elements are referred to the ecliptic and mean equinox of J2000.

Osculating element	Value	Post-fit std. dev.
Eccentricity	0.2796164656	±0.0000000072
Perihelion distance	0.9528518239	±0.0000000071 AU
Time of perihelion	2452034.1012974438 (2001 May 04.60130)	±0.0000019545 Julian day number
Longitude of ascending node	70.9210858275	±0.0000528697 deg
Argument of perihelion	161.0291017983	±0.0000510896 deg
Inclination	1.7279861967	±0.0000005875 deg
Semi-major axis	1.3227007260	±0.0000000142 AU
Orbit period	555.63656111 (1.521223341 yr)	±0.00000893 days

Table 6. Itokawa close approaches. This list of planetary encounters <0.1 AU terminates at the last Earth encounter prior to the linearized 3σ time of close-approach uncertainty (TCA3sg) exceeding ±10 days (14400 min). The span of reliable prediction so-defined is therefore 1793 to 2170, based on the solution #74 data set. "CA dist" is the highest probability approach distance of the reference trajectory to the given body. "MinDist" and "MaxDist" are the 3σ distances from the body at the nominal encounter time. "Vrel" is the nominal relative velocity. Integrations were performed using the DE403 planetary ephemeris and include relativistic perturbations due to the Sun, planets, and Moon, as well as asteroids Ceres, Pallas, and Vesta. The limits of predictability for objects having multiple planetary encounters over centuries will normally be affected by additional factors such as radiation pressure, Yarkovsky acceleration, planetary mass uncertainties, and asteroid perturbations. These factors are not included here, since the relevant physical models are imprecisely defined and key parameters are unmeasured.

Date	Body	CA dist. (AU)	Min. dist. (AU)	Max. dist. (AU)	Vrel (km/s)	TCA3Sg (min)
1793 Jun 28.56041	Earth	0.023689	0.010256	0.057011	6.727	8870.9
1811 Nov 10.83800	Mars	0.078343	0.016444	0.137074	8.216	594.34
1849 Mar 21.47054	Earth	0.081269	0.035147	0.127929	8.340	6566.9
1851 Nov 04.76410	Mars	0.038895	0.022443	0.060531	7.431	1183.5
1852 Apr 09.67893	Earth	0.037141	0.029179	0.057098	5.393	13976.
1855 May 29.66004	Earth	0.053543	0.050331	0.056975	5.115	7662.5
1858 Jun 30.76750	Earth	0.027278	0.017774	0.037076	6.839	2478.0
1859 May 06.39002	Mars	0.094186	0.086735	0.101853	5.625	2060.9
1902 Apr 15.61167	Earth	0.041201	0.040436	0.041992	5.246	875.88
1905 Jun 27.05907	Earth	0.011581	0.011564	0.011599	6.165	40.75
1906 May 24.36393	Mars	0.019701	0.019683	0.019719	6.976	4.80
1920 Dec 17.48373	Mars	0.061055	0.060989	0.061121	5.934	11.13
1940 Apr 10.00983	Earth	0.032526	0.032523	0.032528	5.475	2.50
1943 Jul 04.96046	Earth	0.046786	0.046766	0.046806	7.438	3.80
1970 May 07.70560	Mars	0.069612	0.069604	0.069620	8.179	0.12
1972 May 05.64056	Earth	0.056370	0.056368	0.056373	5.132	9.57
1984 Nov 23.66001	Mars	0.069730	0.069722	0.069739	8.231	0.16
2001 Mar 29.77586	Earth	0.038256	0.038256	0.038256	6.885	0.00
2004 Jun 26.83254	Earth	0.012897	0.012897	0.012897	6.119	0.53
2033 Mar 23.63999	Earth	0.085532	0.085376	0.085688	8.562	20.29
2036 Jun 11.68116	Earth	0.040697	0.040631	0.040762	5.215	73.45
2066 Apr 03.53548	Mars	0.072956	0.072391	0.073522	5.998	97.47
2071 Apr 09.78873	Earth	0.027789	0.027388	0.028206	5.603	373.59
2074 Jul 05.81500	Earth	0.049433	0.047941	0.050920	7.509	275.99
2103 Jun 07.05175	Earth	0.047918	0.046474	0.049405	5.124	2439.6
2122 Sep 12.97517	Mars	0.079906	0.076332	0.083478	8.396	53.58
2135 May 23.60250	Earth	0.057083	0.056091	0.058136	5.138	6612.2
2137 Apr 03.01417	Mars	0.027883	0.021340	0.034517	6.523	519.80
2154 Sep 03.50556	Mars	0.041105	0.032143	0.050316	7.746	11.26
2167 Apr 02.10984	Earth	0.031322	0.022948	0.049369	6.700	5706.1
2169 Mar 27.32431	Mars	0.048397	0.030408	0.067229	6.142	2332.8
2170 Jun 17.22396	Earth	0.036636	0.026889	0.049371	5.275	10694.

In the March 30 Goldstone collage, the radar sees both of the minimum-bandwidths, or "end-on" rotation phases, with the first one presenting a more sharply curved, or "pointy," surface, and the other one presenting a less sharply curved, or "blunter," surface. The Arecibo observations on that day (Fig. 2) overlapped the first part of the Goldstone track and saw just the first of these end-on phases. No striking topographic irregularities are evident in any of our images, although there are brightness patterns that give one the impression of concavities.

SHAPE MODELING

To begin the shape estimation process, we adopted the K+2003 spin vector, which is based on nine months of lightcurve data and, hence, is more precise than pole/period

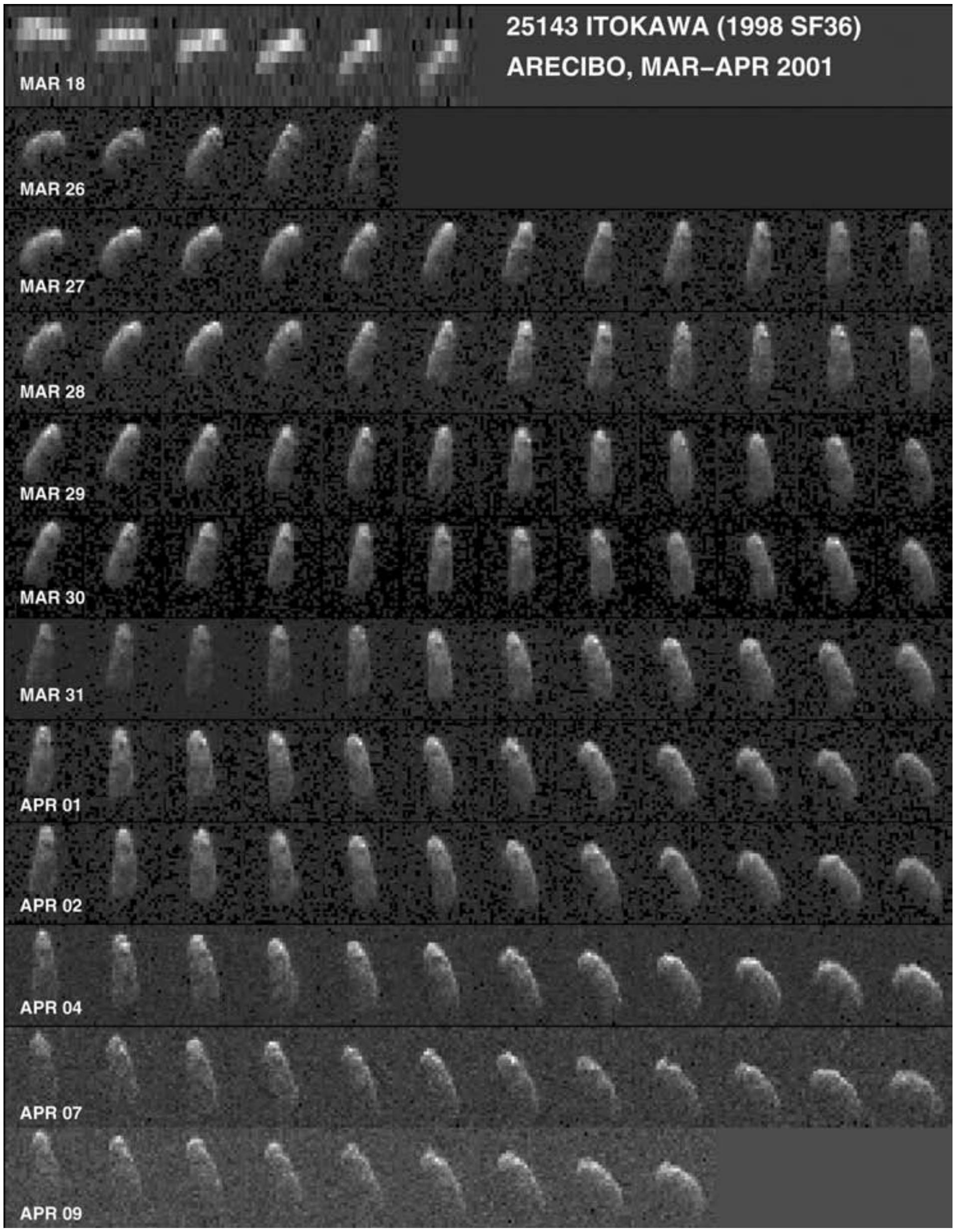

Fig. 2. Arecibo delay-Doppler images of Itokawa. Range (time delay) increases from top to bottom and Doppler frequency increases from left to right, so rotation is counter-clockwise. The collage shows one row of images per date between March 18 (top) and April 9 (bottom). The delay-Doppler resolution is 500 ns (75 m) × 0.0596 Hz on March 18 and 100 ns (15 m) × 0.06482 Hz on the other days. The dimensions of the images are 4500 ns (675 m) × 1.61 Hz on March 18 and 3500 ns (525 m) × 1.62 Hz on the other days. The images show sums of 4–10 runs per panel, spanning intervals of 7–19 min (4° to 9° of rotation), with a median and rms dispersion of 11 ± 3 min (5.2° ± 1.5°). We applied logarithmic contrast stretches on each day to bring out detail near the trailing edges and to avoid saturating pixels near the echo's leading edge. The stretch varies from day to day but is the same for all the images on a given day.

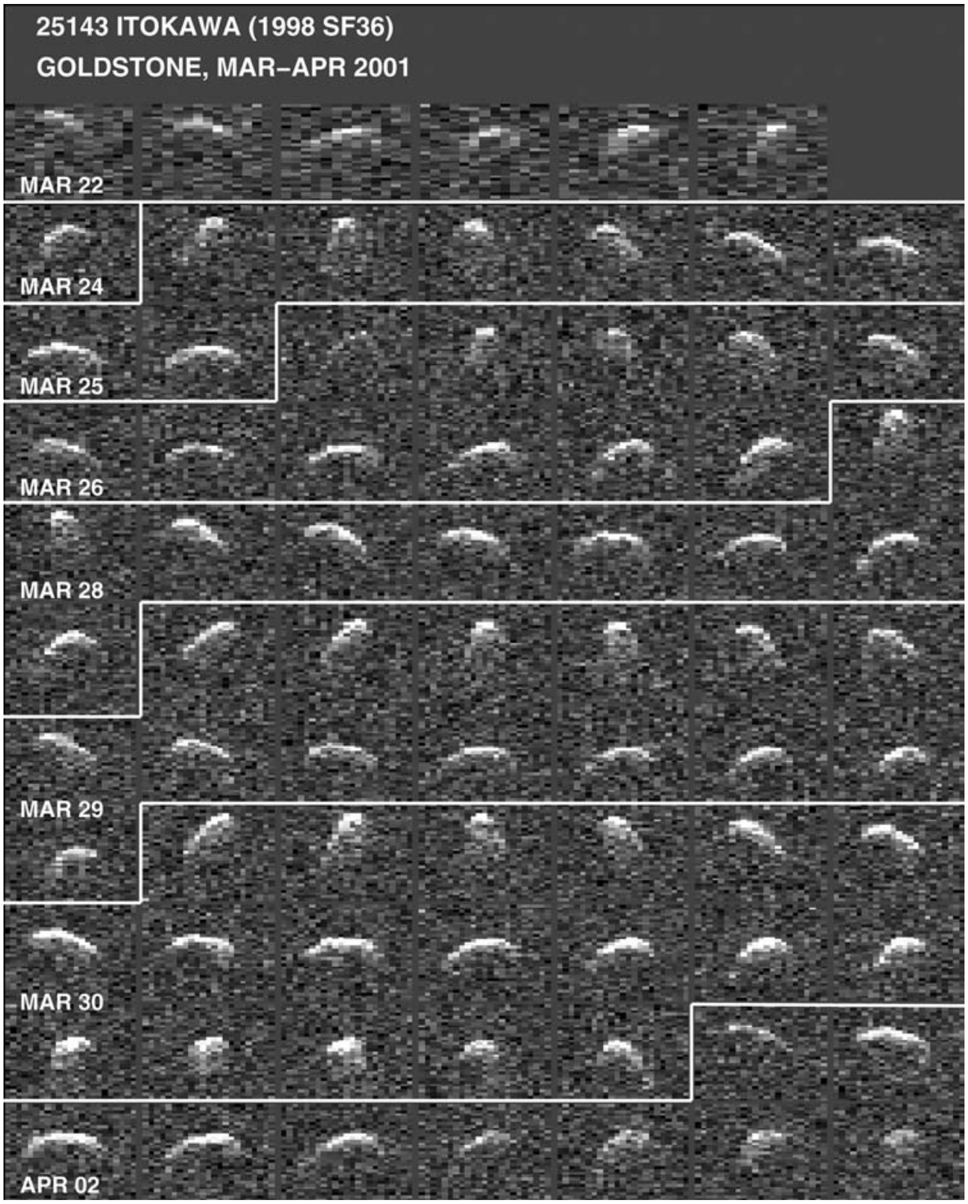

Fig. 3. Goldstone delay-Doppler images of Itokawa. Range (time delay) increases from top to bottom and Doppler frequency increases from left to right, so rotation is counter-clockwise. Images from each date are labeled and are separated by white lines. Each image shows a weighted sum of about 30 min of data, corresponding to about 15° of rotation. Images from March 22 have a resolution of 125 ns (18.75 m) × 0.5 Hz. Images on other days have a resolution of 125 ns (18.75 m) × 0.25 Hz. Images on March 22 have dimensions of 4125 ns (619 m) × 6.5 Hz. Images on other days have dimensions of 4125 ns (619 m) × 5.75 Hz. The images were saturated at 6σ and clipped at -2σ. Due to the varying SNR from day-to-day, the constant saturation level means that the contrast stretch is different for each day.

estimates obtained solely from our three weeks of radar data. Given this spin vector, our visual inspection of the radar images suggested that a first approximation to the asteroid's shape is a biaxial ellipsoid 630 ± 60 m long and 250 ± 30 m wide. We used these results as the starting point in modeling the object.

We used software and procedures developed by Hudson (1993) to estimate Itokawa's shape. As in previous similar analyses (Hudson et al. 2002; Ostro et al. 2000), the procedure was to start by estimating the axis lengths of a triaxial ellipsoid model and then to estimate the shape of a polyhedron parameterized by enough vertices to do a decent job of synthesizing the radar images. (A polyhedron with K vertices has 2K–4 faces and 3K–6 edges.) We found that a polyhedron with 256 vertices (508 triangular faces, with an average area of $[30\ \text{m}]^2$) was adequate in this regard, apparently because this object is not nearly as irregular as, for example, Golevka or Toutatis, for which larger numbers of vertices were needed. We also found that delay-Doppler images synthesized with a 6098-vertex "smoothed version" of the 256-vertex shape are visually indistinguishable from delay-Doppler images synthesized with the 256-vertex model. Since the 6098-vertex model fits the data just as well as the 256-vertex model but looks less artificial, we adopt it here. The 6098-vertex model has 12192 faces and 18288 edges.

Hudson's method minimizes an objective function that consists of the weighted sum of: i) squared residuals between delay-Doppler image pixel values and the corresponding values predicted by the physical model; and ii) penalty functions (Hudson and Ostro 1994, 1995) that can be adjusted to suppress structural features that are not required by the data. For Itokawa, we experimented with weights applied to penalty functions that enforce principal-axis rotation and uniform density distribution, finding no evidence that relaxing these conditions improved the fits. We also penalized structural relief, trying to strike a balance between allowing structure needed to reproduce the appearance of the images and suppressing structure that is not geologically plausible. In other words, there is a strong subjective element in the estimation process.

Table 7 lists our estimates of relevant model parameters. The assigned standard errors, which are subjective, are intended to reflect systematic effects arising in part from the suboptimal imaging coverage. We note that for our shape model, the inversion's root reduced chi-square equals 1.75. This goodness-of-fit statistic would be expected to equal unity if the model contained no systematic errors and the fit were excellent. Differences between our radar images and the images generated from the shape model, most evident near end-on phases, indicate that Itokawa has structural characteristics not reconstructed in our model. In particular, we expect that Itokawa may be slightly more elongated than our model.

Figure 4 shows images obtained at Arecibo on each day and at Goldstone on March 30, along with corresponding images synthesized from the model and plane-of-sky renderings of the 6098-vertex model. Figure 5 shows views of the model along its principal axes, with x, y, and z having the minimum, intermediate, and maximum moments of inertia I_x, I_y, and I_z.

Itokawa's shape can be described as a slightly asymmetrical, slightly flattened ellipsoid about twice as long as it is wide, with topography that is subdued by the standards of other asteroids for which spacecraft images or radar reconstructions are available. The object's pole-on silhouette (the view along the z axis) shows the positive-x end to be fatter and blunter (i.e., less pointed) than the negative-x end. The projection onto the xz plane shows the positive-x side to be more tapered than the negative-x side. In the Goldstone March 30 sequence of Fig. 4, note how the appearance of the radar-facing side of the model at the two end-on phases corresponds to the more pointed and blunted images respectively noted earlier, where the positive-x end looks blunter because the radar, 45° north of the equator, sees the flat top of that end, while the negative-x end looks sharper because the radar-facing side is sharply curved.

Some parts of the asteroid were seen at high echo strength from much more diversified orientations than others. The subradar tracks of our highest resolution (100 ns) images, from Arecibo, are confined to latitudes between +18° and +46° and the less than 40% of a rotation between west longitudes 135°

Table 7. Radar model of Itokawa's characteristics. Parameters are for the 6098-vertex model. Uncertainties are estimated standard errors. The linear resolution of the model is about 30 m. We assumed the values of Kaasalainen et al. (2003) for the sidereal period (12.132 h) and pole direction (ecliptic long., lat. = 355°, –84°), principal-axis rotation (about the z axis in our asteroid-centered coordinate system), and uniform internal density. We also assumed uniform radar scattering properties, with a scattering law of the form $d\sigma/dA = \cos^n\theta_{inc}$, where σ is radar cross section, dA is an element of surface area, and θ_{inc} is angle of incidence; we estimate $n = 2 \pm 1$, which corresponds to Lambertian scattering. The positive side of the longest principal axis (+x) is on the plane of the sky and approaching Earth (the subradar west longitude is 270°) at JD 2451995.53669 = 2001 Mar 27 00:52:50 UTC.

Extents along principal axes:		
(x, y, z)	(548,312,276) m	±10%
Extent ratios:		
x/y	1.756	±15%
y/z	1.130	±15%
area	0.437 km^2	±20%
volume	0.024 km^3	±30%
Ratios of the principal moments of inertia of a uniform-density asteroid with the model's shape:		
I_z/I_x	2.47	±10%
I_y/I_x	2.35	±10%
Equivalent diameter (of a sphere with the model's volume):		
D_{eq}	358 m	±10%
Dimensions of the dynamically equivalent equal-volume ellipsoid (DEEVE, the homogeneous ellipsoid having the same moment-of-inertia ratios and volume as the model):	561 × 304 × 269 m	±10%

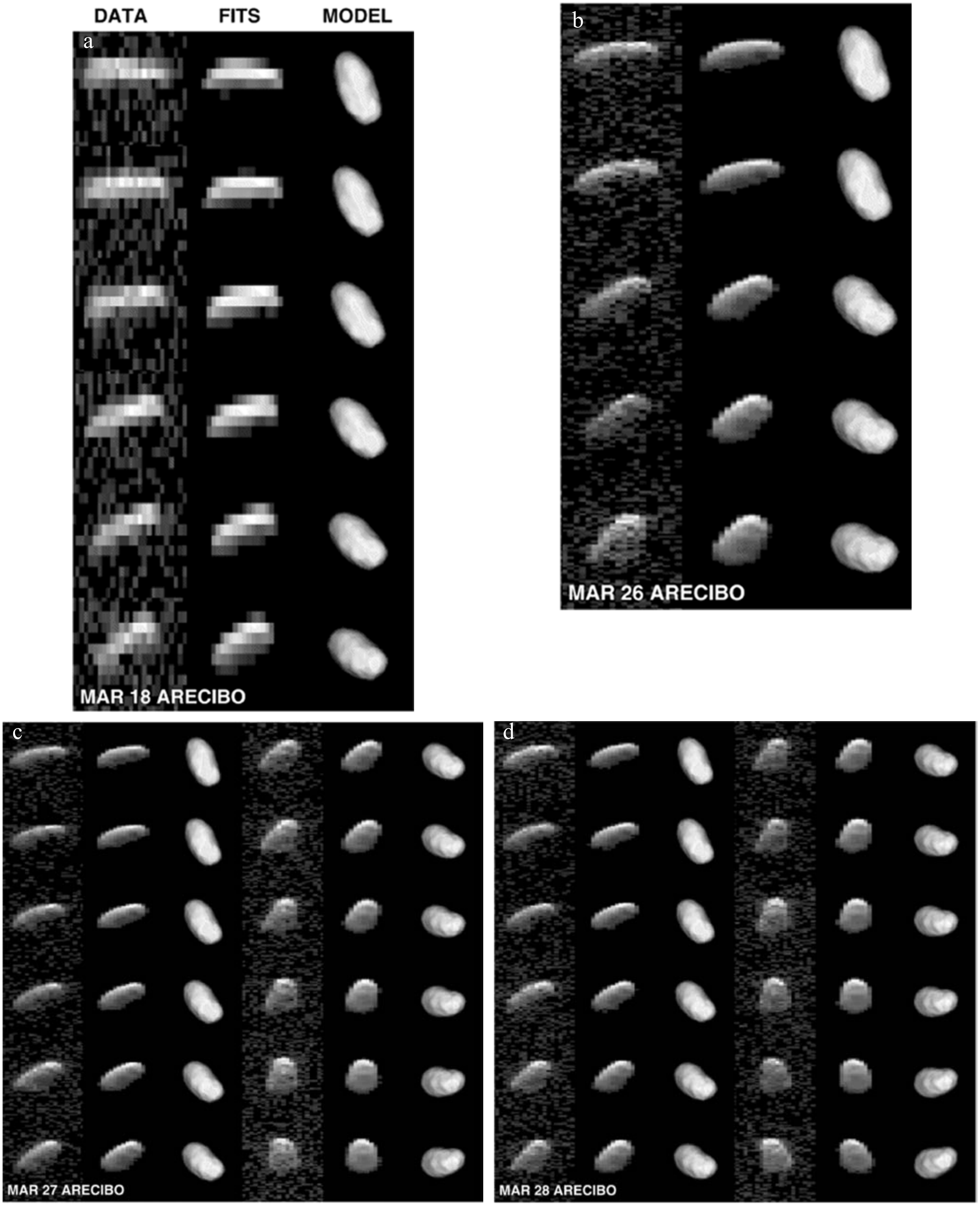

Fig. 4. Itokawa images and model. Each row gives a delay-Doppler data image, the corresponding synthetic image from the model fit, and the corresponding plane-of-sky (POS) rendering of the shape model. In the delay-Doppler frames, the radar is toward the top and rotation is counterclockwise. In the plane-of-sky frames, north is up and east is to the left.

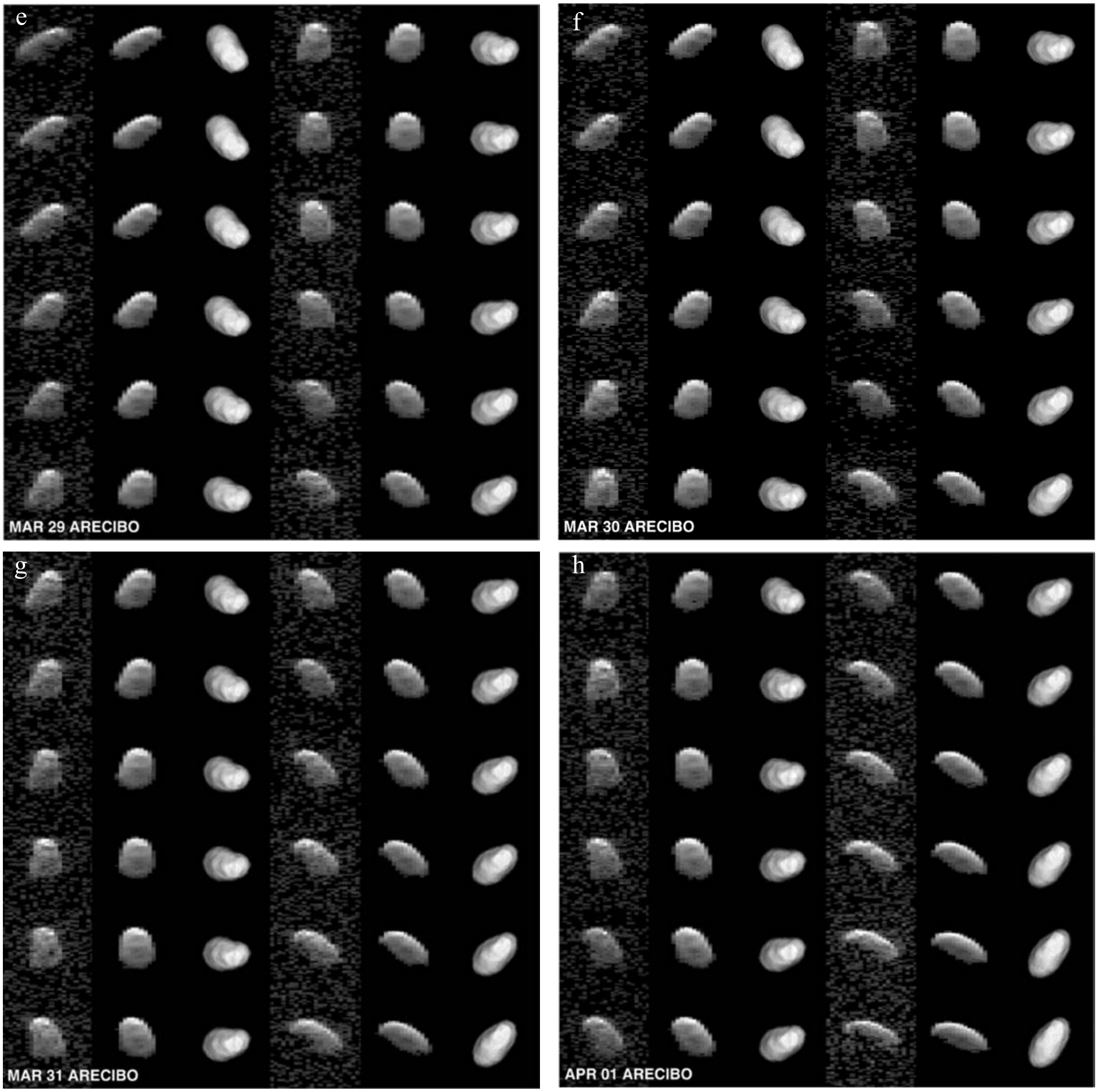

Fig. 4. Itokawa images and model. Each row gives a delay-Doppler data image, the corresponding synthetic image from the model fit, and the corresponding plane-of-sky (POS) rendering of the shape model. In the delay-Doppler frames, the radar is toward the top and rotation is counterclockwise. In the plane-of-sky frames, north is up and east is to the left. *Continued.*

and 276° (Fig. 6). The Goldstone images used in our fits, from March 30, span subradar longitudes not seen from Arecibo, but are much weaker. Consequently, the accuracy of our model should be higher in the vicinity of the Arecibo tracks.

This expectation is borne out Fig. 7, which compares optical lightcurve data (K+2003) to lightcurves synthesized using those authors' model and also to lightcurves synthesized from our radar-derived model. The plot sequence presents 20 lightcurves from the nine-month photometric observation span in 2001. The photometric observations between March 21 and April 1 were made in the mainland U. S. during roughly the same hours as the radar ones (March 21–23: Table Mountain/S. Lowry and P. Weissman; March 28 to April 1: McDonald/T. Farnham). The radar-derived lightcurve provides a good match to the photometry during this period. The March 19 lightcurve was observed from Japan (Mitaka/T. Nakamura et al.), and it covers rotational phases not densely covered by radar.

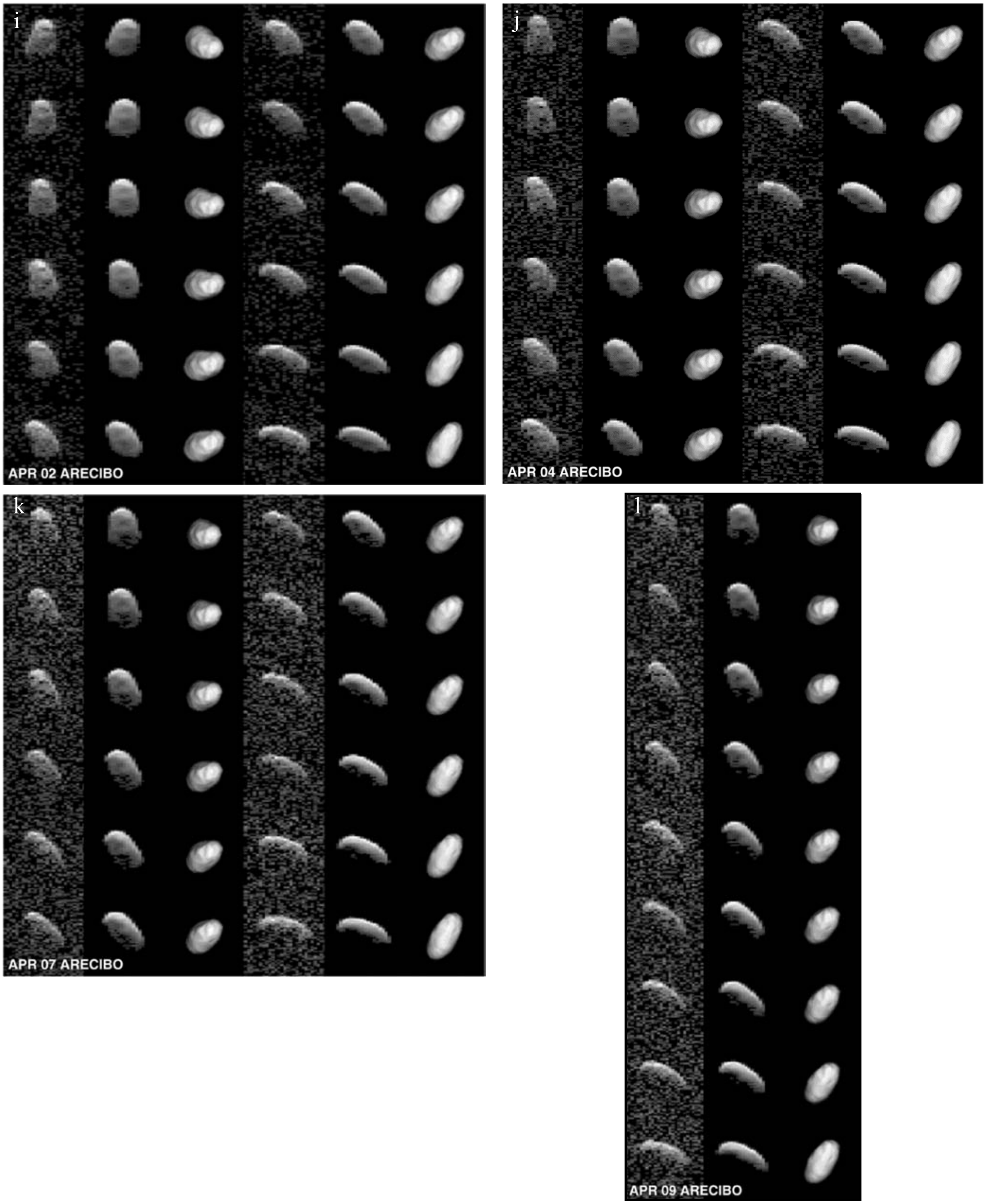

Fig. 4. Itokawa images and model. Each row gives a delay-Doppler data image, the corresponding synthetic image from the model fit, and the corresponding plane-of-sky (POS) rendering of the shape model. In the delay-Doppler frames, the radar is toward the top and rotation is counterclockwise. In the plane-of-sky frames, north is up and east is to the left. *Continued.*

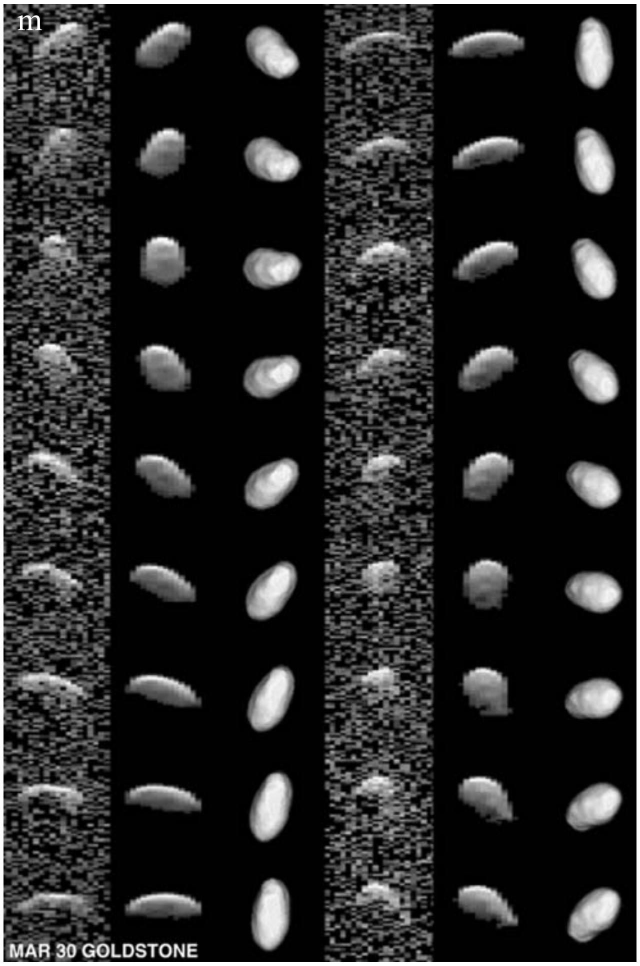

Fig. 4. Itokawa images and model. Each row gives a delay-Doppler data image, the corresponding synthetic image from the model fit, and the corresponding plane-of-sky (POS) rendering of the shape model. In the delay-Doppler frames, the radar is toward the top and rotation is counterclockwise. In the plane-of-sky frames, north is up and east is to the left. *Continued.*

For the rest of the plots, the differences between the two model fits reflect the limited March-April observing geometry that left parts of Itokawa unseen by radar. Likewise, due to the diurnal near resonance, a smaller part on one side of Itokawa's "lower" half remained photometrically unobserved in August and September. (K+2003 discuss the intrinsic limitations of the optical scattering model used in photometric analysis. They also note that their photometric shape model was adjusted to fit the data typically down to the noise level, and that such a fit is necessarily better than that produced by even a perfectly correct shape model. Nonetheless, the similarity between the shapes of our model and the K+2003 convex model is striking.)

SURFACE PROPERTIES

Table 3 lists parameters for Arecibo cw observations and values of radar cross section and SC/OC estimated from the spectra. We obtain mean values of Itokawa's disc-integrated properties: OC albedo = 0.16 ± 0.05, SC/OC = 0.26 ± 0.04. Itokawa's SC/OC and OC radar albedo are, given the uncertainties, indistinguishable from the respective medians of the values available for NEAs (http://echo.jpl.nasa.gov/~lance/asteroid_radar_properties.html). Thus, this asteroid's cm-to-m-scale surface properties may be fairly typical of NEAs. Its SC/OC is comparable to the 13-cm value, 0.22, estimated for Eros (Jurgens and Goldstein 1976, Ostro et al. 1991), suggesting similar structural complexity at cm-to-m scales on these two objects.

Estimates of OC albedo and circular polarization ratio can be used to constrain the bulk density of regolith within about a meter of the surface. Magri et al. (2001) discuss two independent methods for estimating near-surface bulk density; since both methods yield similar results for Itokawa, we present just the output of their "uncalibrated" method, an algorithm based on a mixture of theory, laboratory data, and radar measurements of the Moon and inner planets. This algorithm gives a bulk density and standard errors of 1.66 (+0.35–0.65) g cm^{-3}. Using a more conservative 95% confidence interval, we place an upper bound of 2.4 g cm^{-3} on the surface bulk density.

The mean surface bulk density and standard deviation for the 19 radar-detected S-class targets analyzed by Magri et al. (2001) are 1.8 ± 0.5 g cm^{-3}; Itokawa is fairly typical in this regard. If this asteroid is chondritic with solid density ~3.6 g cm^{-3} (Britt and Consolmagno 2003), the bulk density obtained here implies a near-surface porosity greater than 30% at the 95% confidence level (see discussion in Magri et al. 2001).

Figure 8 shows results of dividing each pixel's SC power by its OC power in March 28–30 images. SC/OC varies across each image, with the lowest values clustered near the leading edge and the largest values toward the trailing edge. We understand this pattern, which was also seen on Toutatis (Ostro et al. 1999) and 1999 JM8 (Benner et al. 2002), as due to OC echo from smooth surface elements that face the radar preferentially where the mean surface is normal to the line of sight.

Much of the Ostro et al. (1999) analysis of Toutatis' radar signature (SC/OC = 0.29, OC albedo = 0.24) is applicable to Itokawa. They argued that multiple scattering from buried rocks probably does not make a significant contribution to the echoes because the radar is unlikely to penetrate much more than ten wavelengths into the regolith. They interpreted the asteroid's disc-integrated radar properties in terms of a smooth component partially covered by rocks (at least as large as a centimeter, using an admittedly simplistic approach intended to provide first-order constraints on p, the porosity of the smooth component, and C, its fractional coverage by rocks. Let us assume that Itokawa is made of material with a solid (grain) density of 3.75 g cm^{-3}. Then the Ostro et al. approach suggests that Itokawa's smooth surface component has a bulk density of 1.9 g cm^{-3}, a porosity $p = 0.5 \pm 0.2$ that

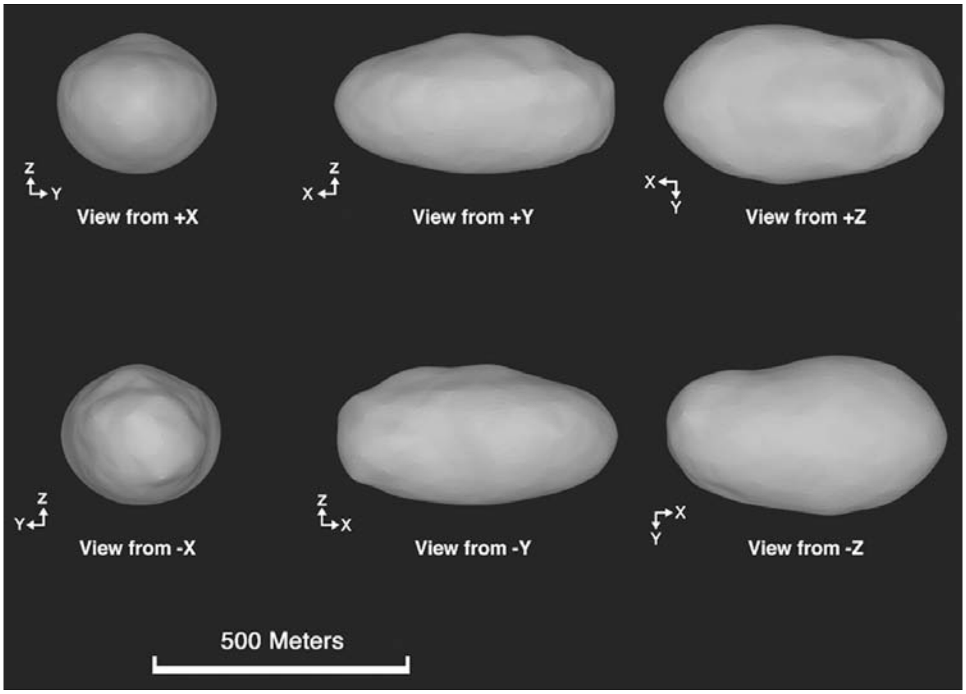

Fig. 5. Views of our Itokawa model along its principal-axis directions. This rendering uses a Lambertian backscattering law, as estimated in our shape reconstruction. See Table 7.

is similar to lunar regolith values (Carrier et al. 1973), and a rock coverage $C = 0.36 \pm 0.15$. If Itokawa's volume consists of 64% smooth component and 36% rocks, then the interpretive approaches described in this section imply a value for the asteroid's bulk density of about 2.5 g cm^{-3}.

GRAVITATIONAL ENVIRONMENT

Let us use the radar-derived shape model and adopt a bulk density of 2.5 g cm^{-3} (and hence a mass of 6.0×10^{13} g) to examine Itokawa's gravitational environment. First, following the methodology outlined in Scheeres et al. (1996), we can compute the gravitational slope over the surface of the asteroid, the total gravitational plus centripetal accelerations over the body, and the launch speeds leading ejecta to either return to the asteroid or escape from it.

Itokawa has a very relaxed surface, with gravitational slopes (Fig. 9) nowhere steeper than 27°, which is less than typical angles of repose for unconsolidated granular material. The average slope is 9° and 95% of the surface has slopes shallower than 18°.

Itokawa's total (gravitational + rotational) surface acceleration varies by 24%, from a minimum of 1.00×10^{-4} m s^{-2} to a maximum of 1.24×10^{-4} m s^{-2} (1.0×10^{-5} to 1.3×10^{-5} times the gravitational acceleration at the Earth's surface). The ranges of this acceleration's normal component (0.92×10^{-4} to 1.24×10^{-4} m s^{-2}) and tangential component (0 to 0.47×10^{-4} m s^{-2}) matter if electrostatic forces are involved in the motion of surface particles.

The fate of a particle (or a spacecraft, or a person) launched from a given location on the surface depends on the launch speed and direction. We define the necessary launch speed at any surface location as the minimum speed a particle must have if it is to escape; lower speeds guarantee return. Itokawa's necessary speeds range from 12.7 to 16.5 cm s^{-1}. We define the sufficient launch speed at any surface location as the minimum speed a particle must be given perpendicular to the surface if escape is to be guaranteed. Sufficient launch speeds range from 17.1 to 24.6 cm s^{-1}.

For a near-ellipsoidal body such as Itokawa there will be four synchronous orbits, corresponding to true circular orbits with the period exactly equal to the rotation period (Scheeres 1994, Scheeres et al. 1996). These orbits appear as stationary points in the (rotating) body-fixed frame and will lie close to the equatorial principal axes of the body's inertia ellipsoid. For Itokawa these points all lie from 0.57 to 0.60 km from its center of mass (from 0.42 to 0.33 km from its surface, respectively) and are all unstable, making Itokawa a "Type II" object (Scheeres 1994). This suggests that motion near this asteroid will be subject to destabilizing influences from the gravity field, with the exception of retrograde orbits with inclinations close to 180° (Scheeres et al. 2000).

DETECTABILITY OF YARKOVSKY ACCELERATIONS

The Yarkovsky effect, a very subtle nongravitational phenomenon involving acceleration of a rotating object due to

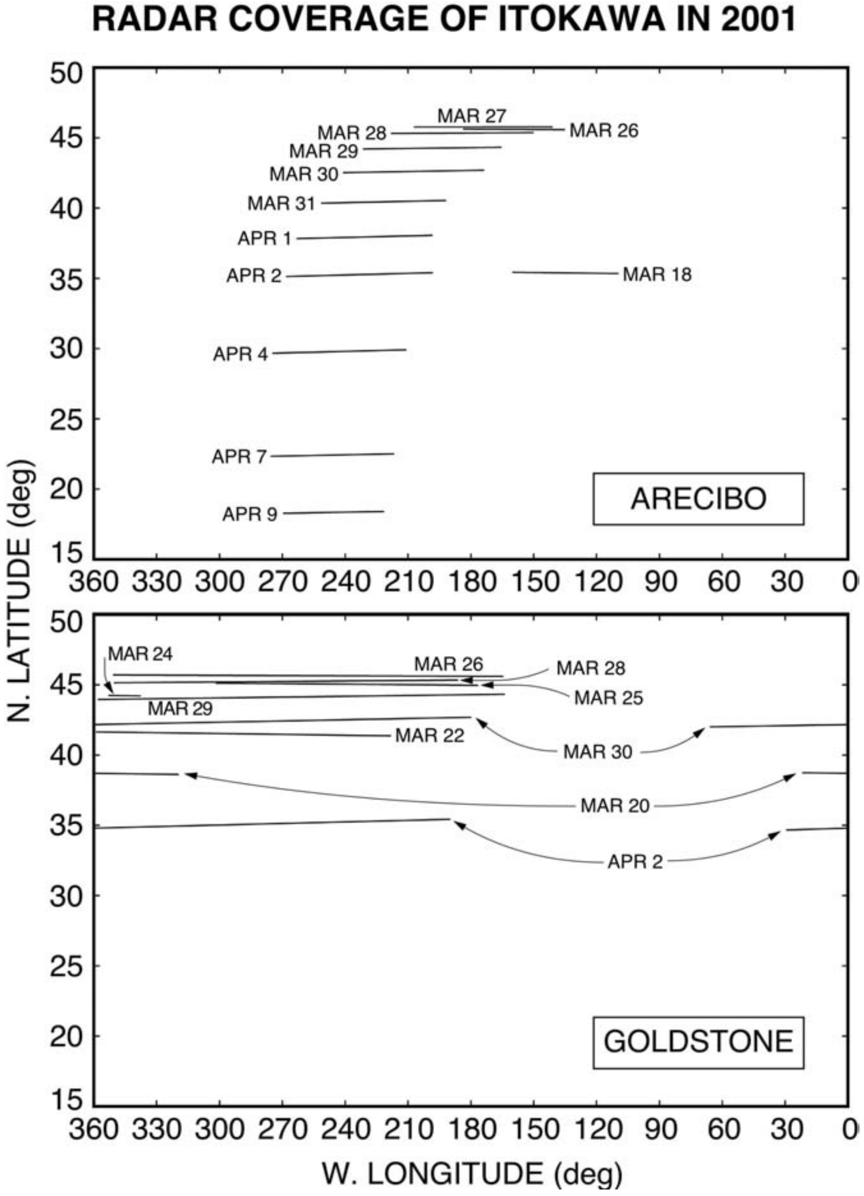

Fig. 6. Subradar tracks of the 2001 March-April Arecibo and Goldstone imaging data sets on our Itokawa model. Rotation is about the model's shortest principal axis (z). The +x axis passes through the zero meridian. West longitude increases as the asteroid rotates. The lightcurve-derived spin period (12.132 hr) and pole direction (ecliptic long., lat. = 355°, –84°) of Kaasalainen et al. (2003) are assumed.

its anisotropic thermal emission of absorbed sunlight, can cause an object's orbit to undergo semimajor axis drift (Rubincam 1995; Farinella et al. 1998; Bottke et al. 2000). Vokrouhlický et al. (2000) predicted that radar-refined orbits with sufficiently long astrometric time bases could permit detection of nongravitational acceleration of NEAs due to the Yarkovsky effect, and such a detection was recently achieved for 6489 Golevka (Chesley et al. 2003). We have explored opportunities to detect Yarkovsky acceleration of Itokawa, following Vokrouhlický et al. (2000), taking into consideration the physical characteristics of Itokawa, including quantities derived from our shape model as well as results of IR observations by Ishiguro et al. (2003).

We find that the current radar + optical astrometric dataset does not allow unambiguous detection of the Yarkovsky effect during Itokawa's close approach in June 2004. However, if radar ranging to Itokawa during that apparition is successful, then fine-precision range-Doppler tracking of the Hayabusa spacecraft during its 2005 Itokawa encounter would have excellent prospects for detecting the effect, because of the pronounced difference between the Yarkovsky- included and no-Yarkovsky orbit predictions during May–November 2005 (Fig. 10), and because the spacecraft's telemetry system (7156.533-MHz uplink, 8408.210-MHz downlink) can make measurements with precision as fine as 0.1 mm s^{-1} and 10 m. Hayabusa will not

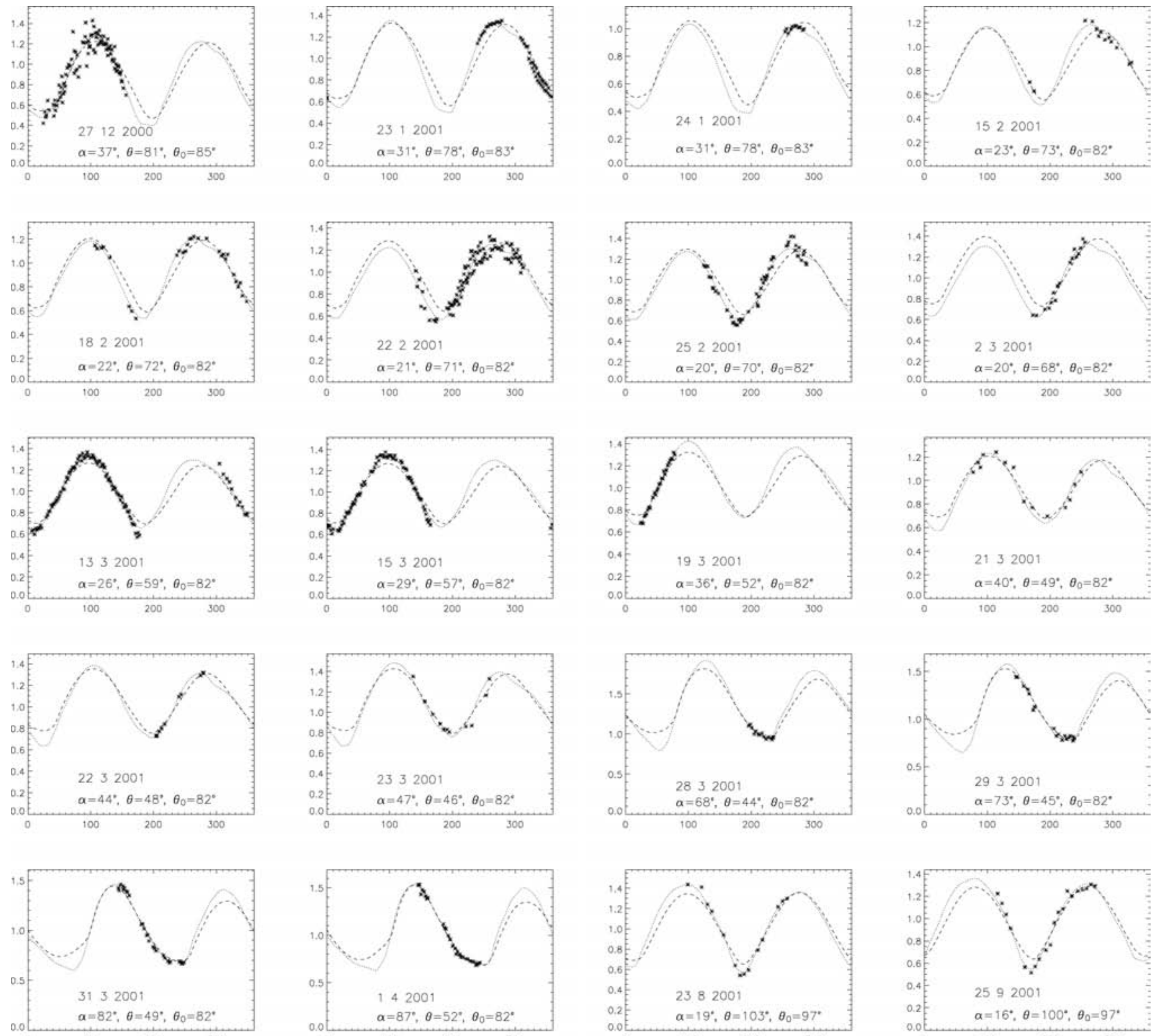

Fig. 7. Optical lightcurve data (asterisks) from Kaasalainen et al. (2003), lightcurves synthesized using those authors' shape model (dotted curves), and lightcurves synthesized using our shape model (dashed curves). Both models use the Kaasalainen et al. (2003) spin period and pole direction. The horizontal axes give the rotational phase (west longitude) in degrees, and the vertical axes give brightness in units of relative intensity. In each frame, we give the viewing aspect θ (measured from the pole), the illumination aspect θ_0, and the solar phase angle α. The light-scattering model is a weighted combination of the Lommel-Seeliger and Lambert laws with respective weights of 0.9 and 0.1, as used by Kaasalainen et al. (2003). Similar fits and model are obtained with S-type Hapke parameters (Helfenstein and Veverka 1989).

orbit the asteroid, but instead will hover along the asteroid-sun line, and therefore Earth-Itokawa ranging may have effective noise values as large as 100 m, but this still should be more than adequate for a Yarkovsky detection.

After the Itokawa encounter, the asteroid's mass and volume should be fairly well known. Also, the MINERVA surface hopper will have four probes to directly measure the surface temperatures wherever it sets down on the surface, strongly constraining the thermal conductivity. The magnitude of the Yarkovsky acceleration depends strongly on the asteroid's mass and surface thermal conductivity, so the Hayabusa measurements should clarify what really is needed to decouple those parameters.

CONCLUSION: PROSPECTS FOR IMPROVING OUR MODEL

The orientational coverage of our strongest images is more limited than for most other radar-derived 3-D models. The effect of this limitation on the reconstruction's accuracy depends strongly on the asteroid's detailed physical characteristics and is difficult to quantify. Similarly, although

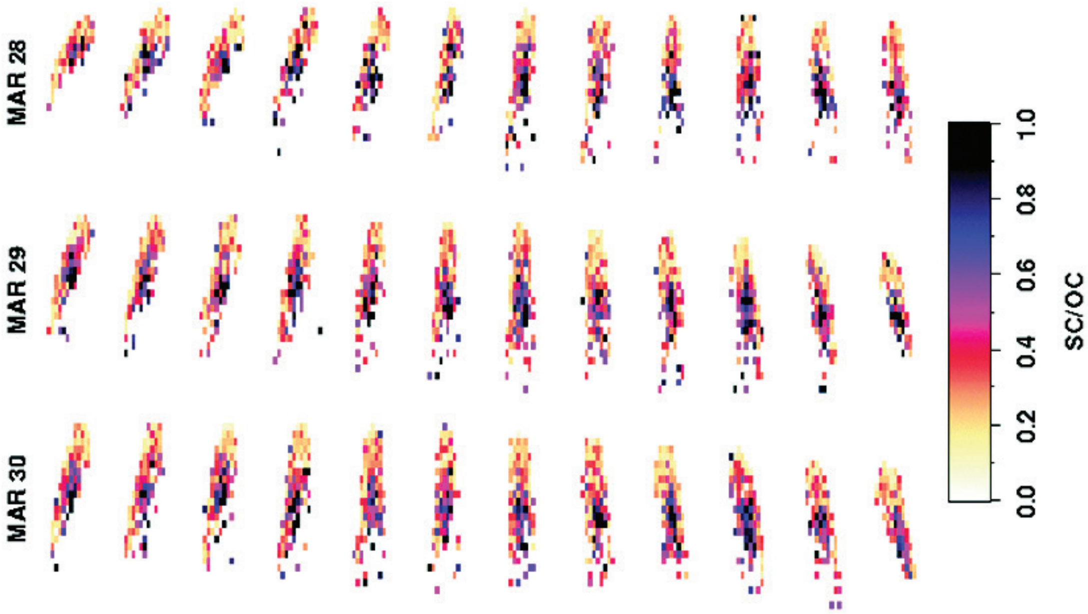

Fig. 8. Arecibo polarization ratio (SC/OC) images of Itokawa from March 28, 29, 30. The range (time delay) increases from top to bottom and the Doppler frequency increases from left to right, so rotation is counterclockwise. Delay-Doppler resolutions, dimensions, and sums of runs are the same as in Fig. 2. SC/OC is plotted by adopting a 3σ detection threshold. Weaker pixels are mapped to white. The color stretch is saturated at SC/OC = 1.0 (black) to emphasize the most interesting regions of the dynamical range.

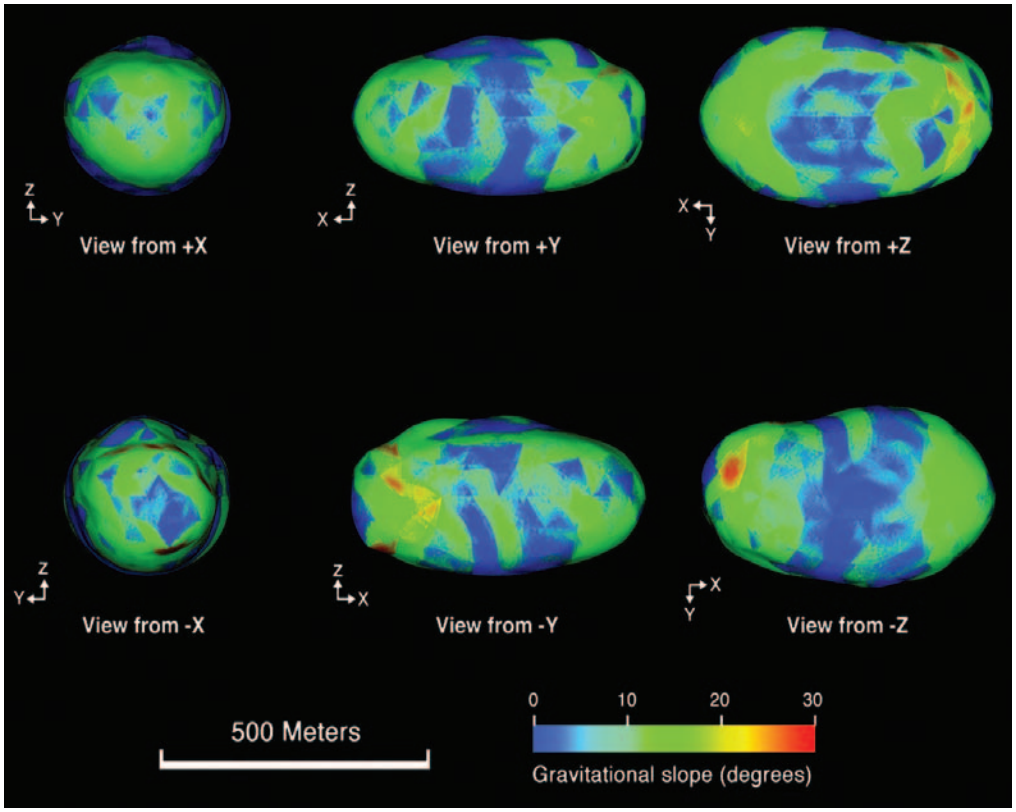

Fig. 9. Gravitational slopes on our Itokawa model.

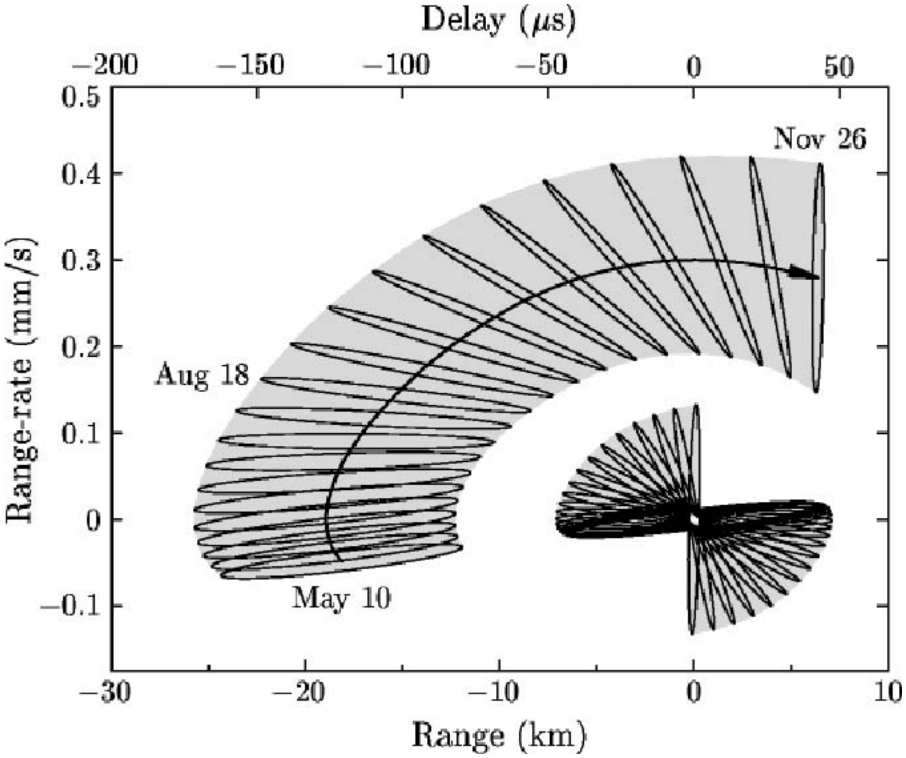

Fig. 10. Range and range-rate predictions and their uncertainty ellipses for Itokawa's orbit during dates in 2005 when the asteroid is to be visited by the Hayabusa spacecraft. The origin corresponds to the nominal orbital solution without any Yarkovsky perturbation. Ellipses offset from the origin include predicted Yarkovsky accelerations. Ellipses, shown every ten days, depict the 95% confidence level of the solution, with the uncertainty due to the propagation of optical and radar astrometric errors; our simulation assumed that delay-Doppler astrometry during the 2004 apparition will have formal uncertainties of 150 ns and 0.06 Hz, similar to those acquired in 2001 (Table 4). The ellipses rotate clockwise during this 200-day period. The shaded areas are swept by the 95% confidence zones. The upper abscissa indicates the roundtrip time delay corresponding to the range offset on the lower abscissa.

non-principal-axis (NPA) rotation is not evident either in our analysis or in the photometric analysis of Kaasalainen et al. (2003), we certainly cannot rule out a small NPA component to Itokawa's rotation that is not detectable in our modeling procedure.

Fortunately, Itokawa's June 2004 close approach will bring it within 0.013 AU from Earth, about one-third of its 2001 minimum distance, so radar echoes obtainable from Goldstone will be stronger than the 2001 Arecibo echoes. The longitude coverage of radar images should be thorough, and the subradar latitude trajectory during favorable radar dates will pass from near equatorial to tens of degrees south, permitting coverage that will supplement what we obtained in 2001. A similar statement applies to prospects for photometric coverage of the asteroid in 2004. We expect 2004 observations to permit significant refinement of the model presented here. Indeed, Itokawa will be an important "ground truth" asteroid after the Hayabusa mission, having been well-observed both photometrically and with radar imaging.

Acknowledgments–We thank Scott Hudson for providing his shape reconstruction software. We thank the technical staffs at Arecibo and Goldstone for help with the observations. We are grateful to the following JPL projects for relinquishing time on DSS-14 so we could observe Itokawa at rotation phases inaccessible to Arecibo: Galileo, Groundbased Radio Astronomy, Space VLBI, Voyager 1, Orbital Debris Radar, Mercury Relativity Radar, and DSN Maintenance. Some of our Arecibo observations used the Caltech Baseband recorder (CBR), whose development and fabrication was funded by the National Science Foundation. S. Ostro was partially supported by the JPL MUSES-C Project and the Steven and Michele Kirsch Foundation. D. J. Scheeres was partially supported by NASA's Planetary Geology and Geophysics program through a grant to The University of Michigan. C. Magri was partially supported by NSF grant AST-0205975. Part of this research was conducted at the Jet Propulsion Laboratory, California Institute of Technology, under contract with the National Aeronautics and Space Administration (NASA). The Arecibo Observatory is part of the National Astronomy and Ionosphere Center, which is operated by Cornell University under a cooperative agreement with the National Science Foundation and with support from NASA.

Editorial Handling—Dr. Carlé Pieters, Dr. Anita Cochran

REFERENCES

Binzel R. P., Rivkin A. S., Bus S. J., Sunshine J. M., and Burbine T. H. 2001. MUSES-C target asteroid (25143) 1998 SF36: A reddened ordinary chondrite. *Meteoritics & Planetary Science* 36:1167–1172.

Bottke W. F., Jr., Rubincam D. P., and Burns J. A. 2000. Yarkovsky thermal forces. *Icarus* 145:301–331.

Britt D. T. and Consolmagno G. J. 2003. Stony meteorite porosities and densities: A review of the data through 2001. *Meteoritics & Planetary Science* 38:1161–1180.

Carrier W. D., III, Mitchell J. K., and Mahmood A. 1973. The relative density of lunar soil. Proceedings, 4th Lunar and Planetary Science Conference. pp. 2403–2411.

Chesley S. R., Ostro S. J., Vokrouhlický D., Čapek D., Giorgini J. D., Nolan M. C., Hine A. A., Margot J. L., Benner L. A. M., and Chamberlin A. B. 2003. Direct detection of the Yarkovsky effect via radar ranging to near-Earth asteroid 6489 Golevka. *Science* 302:1739–1742

Dermawan B., Nakamura T., Fukushima H., Sato H., Yoshida F., and Sato Y. 2002. CCD photometry of the MUSES-C mission target: Asteroid (25143) 1998 SF36. *Publications of the Astronomical Society of Japan* 54:635–640.

Farinella P., Vokrouhlický D., and Hartmann W. K. 1998. Meteorite delivery via Yarkovsky orbital drift. *Icarus* 132:378–387.

Helfenstein P. and Veverka J. 1989. Physical characterization of asteroid surfaces from photometric analysis. In *Asteroids II,* edited by Binzel R. P., Gehrels T., and Matthews M. S. Tucson: University of Arizona Press. pp. 557–593.

Hudson S. 1993. Three-dimensional reconstruction of asteroids from radar observations. *Remote Sensing Reviews* 8:195–203.

Hudson R. S. and Ostro S. J. 1994. Shape of asteroid 4769 Castalia (1989 PB) from inversion of radar images. *Science* 263:940–943.

Hudson R. S. and Ostro S. J. 1995. Shape and non-principal-axis spin state of asteroid 4179 Toutatis from radar images. *Science* 270: 84–86.

Hudson R. S., Ostro S. J., Jurgens R. F., Rosema K. D., Giorgini J. D., Winkler R., Rose R., Choate D., Cormier R. A., Franck C. R., Frye R., Howard D., Kelley D., Littlefair R., Slade M. A., Benner L. A. M., Thomas M. L., Mitchell D. L., Chodas P. W., Yeomans D. K., Scheeres D. J., Palmer P., Zaitsev A., Koyama Y., Nakamura A., Harris A. W., and Meshkov M. N. 2000. Radar observations and physical modeling of asteroid 6489 Golevka. *Icarus* 148:37–51.

Ishiguro M., Abe M., Ohba Y., Fujiwara A., Fuse T., Terada H., Goto M., Kobayashi N., Tokunaga A.T., and Hasegawa S. 2003. Near-infrared observations of MUSES-C mission target. *Publications of the Astronomical Society of Japan* 55:691–699.

Jurgens R. F. and Goldstein R. M. 1976. Radar observations at 3.5 and 12.6 cm wavelength of asteroid 433 Eros. *Icarus* 28:1–15.

Kaasalainen M., Kwiatkowski T., Abe M., Piironen J., Nakamura T., Ohba Y., Dermawan B., Farnham T., Colas F., Lowry S., Weissman P., Whiteley R. J., Tholen D. J., Larson S. M., Yoshikawa M., Toth I., and Velichko F. P. 2003. CCD photometry and model of MUSES-C target (25143) 1998 SF36. *Astronomy and Astrophysics* 405:L29–L32.

Magri C., Consolmagno G. J., Ostro S. J., Benner L. A. M., and Beeney B. R. 2001. Radar constraints on asteroid regolith compositions using 433 Eros as ground truth. *Meteoritics & Planetary Science* 36:1697–1709.

Ostro S. J., Campbell D. B., Chandler J. F., Shapiro I. I., Hine A. A., Velez R., Jurgens R. F., Rosema K. D., Winkler R., and Yeomans D. K. 1991. Asteroid radar astrometry. *Astronomical Journal* 102:1490–1502.

Ostro S. J., Hudson R. S., Nolan M. C., Margot J. L., Scheeres D. J., Campbell D. B., Magri C., Giorgini J. D, and Yeomans D. K. 2000. Radar observations of asteroid 216 Kleopatra. *Science* 288: 836–839.

Ostro S. J., Hudson R. S., Benner L. A. M., Nolan M. C., Giorgini J. D., Scheeres D. J., Jurgens R. F., and Rose R. 2001. Radar observations of asteroid 1998 ML14. *Meteoritics & Planetary Science* 36:1225–1236.

Rubincam D. P. 1995. Asteroid orbit evolution due to thermal drag. *Journal of Geophysical Research* 100:1585–1594.

Scheeres D. J. 1994. Dynamics about uniformly rotating tri-axial ellipsoids: Applications to asteroids. *Icarus* 110:225–238.

Scheeres D. J., Ostro S. J., Hudson R. S., and Werner R. A 1996. Orbits close to asteroid 4769 Castalia. *Icarus* 121:67–87.

Scheeres D. J., Williams B. G., and Miller J. K. 2000. Evaluation of the dynamic environment of an asteroid: Applications to 433 Eros. *Journal of Guidance, Control, and Dynamics* 23:466–475.

Sekiguchi, T., Abe M., Boehnhardt H., Dermawan B., Hainaut O. R., and Hasegawa S. 2003. Thermal observations of MUSES-C mission target (25143) 1998 SF36. *Astronomy and Astrophysics* 397:325–328.

Vokrouhlický D., Milani A., and Chesley S. R. 2000. Yarkovsky effect on small near-Earth asteroids: Mathematical formulation and examples. *Icarus* 148:118–138.